Temperature- and Process-Robust Frequency Encoding for a VCO-Based Neural Front End with Body-Coupled Communication: A Model-Based Study

Nithin Purushothama

nithinpurushothama@gmail.com • interactive model and full report: `https://nithinpuru.com/vco-bcc/`

November 2026

Abstract

The neural front end of Meimandi *et al.* [1] occupies 0.0025 mm^2 on the tip of a microcatheter and transmits the neural signal through the body as the frequency of a 3-stage current-starved ring oscillator, so that the loss of the body channel does not reduce the signal itself. Its behaviour over temperature, supply and process is left to future work. This work presents a behavioural model of the complete chain, validated against the published carrier, noise and dynamic range, together with transistor-level rebuilds of the ring and its drive in SKY130. The model identifies one dominant limitation: the control transistors of the ring operate in weak inversion, so the carrier is exponential in the threshold voltage. With the published linear read-out, the gain drifts by 4.0 %/°C, the centre frequency spreads by a factor of 27.3 across five process corners, and a 1 % supply change appears as 42 µV at the input. Three principal techniques are proposed and evaluated in the same models. A resistor-defined voltage-to-current drive for the same ring (**P10**) reduces the corner spread to 1.35 and the temperature coefficient of the centre frequency from 7.05 to 0.22 %/°C. Reading the carrier as $\ln f$ (**P2**), and as $\ln(f_A/f_B)$ with a second ring on the other LNA output (**P4**), reduces the gain drift to 0.31 %/°C and the supply pick-up by 44 dB; **P2** alone requires no change to the implant. A phase-locked loop per carrier (**P5**) instead of zero-crossing counting maintains a spike-detection F1 score of 0.99 instead of 0.82 at 80 dB of channel loss. Further techniques provide an in-situ gain calibration from a carrier-locked test tone (**P11**), frequency-division access for 15 implants (**P6**) and an implant fingerprint (**P7**). All results are obtained from simulation; nothing is measured.

Index Terms: body-coupled communication, current-starved ring oscillator, frequency modulation, neural recording, phase-locked loop, temperature compensation, VCO-based front end.

Table 1: Proposed techniques, in order of significance. Improvements are model results relative to the published design.

	Technique	Principle	Modelled improvement	Overhead
P10	Resistor-defined V-to-I drive	A source-degenerated pair with a resistor tail replaces the load-balancing amplifier and M27/M28, so that a resistor, not the threshold voltage, sets the ring current	Corner spread of f_0 from 27.3× to 1.35×; temperature coefficient from 7.05 to 0.22 %/°C; nonlinearity from 30.5 to 1.18 %	About 430 µm^2 of poly resistor; current 1.73 to 1.42 µA
P2	Logarithmic read-out	The receiver computes $\ln f$ instead of $(f-\bar{f})/K$; for an exponential ring the slope of $\ln f$ does not depend on f_0	Gain drift from 4.0 to 0.31 %/°C; THD of a 1 mV_{pp} tone from 15.9 to 1.7 %	None on the implant
P4	Two rings, ratio read-out	A second ring driven by the other LNA output; the receiver computes $\ln(f_A/f_B) = 2kv$, so that common shifts cancel	Supply pick-up 44 dB lower; gain spread over 24 chips from 5.6 to 0.41 %	One more ring; two carriers share the output drive
P5	PLL per carrier	A second-order digital PLL after a complex down-mix replaces zero-crossing counting	Highest loss with F1 $\geq$ 0.9 from 75 to 80 dB; with **P2**, **P4**: F1 at 80 dB from 0.82 to 0.99	Receiver logic only
P11	Carrier-locked test tone	A ±25 µV tone at the carrier divided by 256 re-measures K_{vf} and the electrode impedance during recording	K_{vf} within 1.19 % in 1 s and 0.24 % in 3 s; spike F1 0.989 with the tone removed	Divider and switch on the implant
P6	Narrow deviation	Diode-stage gain reduced by 8 for frequency-division access	Implants in 100 kHz to 1 MHz from 1 to 15	VCO noise 8× larger at the input
P7	Implant fingerprint	The ratio of the two carriers at rest is set by mismatch and is temperature-stable	88 % of 24 chips identified across 4 °C (one ring: 4 %)	None beyond **P4**

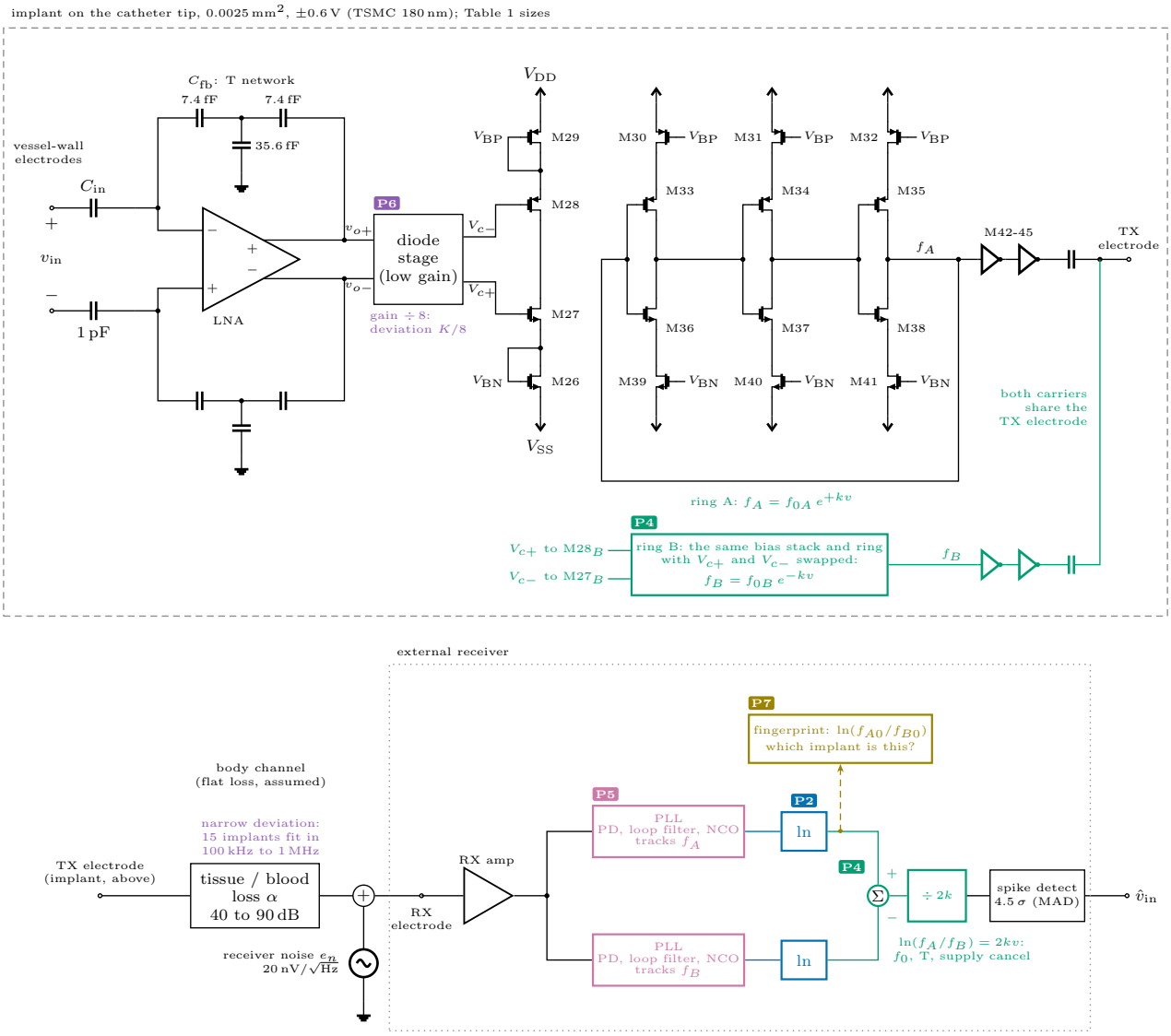


Figure 1: Proposed link: the published front end [1] (black; LNA with the T-capacitor feedback, diode stage, bias stack M26 to M29, current-starved ring M30 to M41 and output stage, Table 1 devices) with the receiver-side techniques in colour. Top: the implant. Bottom: the body channel and the external receiver. **P4** adds a second ring with the control inputs swapped, **P2** reads both carriers as $\ln f$, **P5** tracks each carrier with a PLL, **P6** lowers the deviation and **P7** identifies the implant. The implant-side technique **P10** replaces the drive of each bias stack (Fig. 3).

1 Introduction

Body-coupled communication lets an implant transmit through the tissue itself, without an antenna or a coil. In [1], a fully differential capacitive-feedback LNA drives a 3-stage current-starved ring oscillator through a diode stage and a bias stack (M26 to M29), and an output stage drives the carrier into the blood through a 100 µm² electrode. The neural signal is carried as frequency, with a conversion gain K_{vf} of 347 Hz/µV around a 245 kHz carrier, a band of 6 Hz to 6.7 kHz, 5.55 μV_{rms} of noise in the spike band and 42.1 dB of dynamic range. The receiver reads the frequency by counting zero crossings and removes f_0 by tracking the carrier mean; K_{vf} is corrected per device, and full characterisation over temperature and supply is left to future work.

This work examines how that frequency code behaves when the vessel temperature, the supply and the process vary, by means of two behavioural models and SKY130 transistor-level rebuilds, and evaluates the techniques of Table 1 in the same models. Sec. 2 describes the models and their validation, Sec. 3 the limitation they reveal, Sec. 4 the proposed techniques and Sec. 5 the limits of this study.

Table 2: Published design and proposed techniques in the same models. Corner and temperature rows: SKY130 at ±0.6 V with the Table 1 sizes; gain, supply and link rows: behavioural model with SKY130 sensitivities at ±0.9 V. Simulation only.

Metric	Published design (model)	Proposed	By
Centre-frequency spread, five SKY130 corners [max/min]	27.3×	1.35×	**P10**
Centre-frequency temperature coefficient [%/°C]	7.05	0.22	**P10**
Tuning nonlinearity over ±0.3 V [% of span]	30.5	1.18	**P10**
Read-out gain drift with temperature [%/°C]	4.0	0.31	**P2**
Gain change for a 2 °C warmer vessel, end to end [%]	7.2	0.6	**P2**, **P4**
Input-referred error for a 1 % supply change [µV]	42	0.26	**P4**
1 mV of 50 Hz ripple on the rails, input-referred [μV_{pk}]	6.9	0.10	**P4**
Highest channel loss with spike F1 ≥ 0.9 [dB]	75	80	**P2**, **P4**, **P5**
Supply current of the ring and its drive [µA]	1.73	1.42	**P10**
Ring oscillators on the implant	1	2	**P4**
Spike F1 at 85 dB of loss (both below 0.9)	0.45	0.29	**P4**, **P5**

2 Behavioural Model and Validation

The chain is modelled in signal order. The input is a synthetic recording of three units (60 to 300 µV, biphasic, Poisson firing) on a $1/f$ local field potential. The LNA has the published band and an input-referred noise spectrum $S(f) = a + c/f^g$ fitted to the published 15.5 and 5.55 μV_{rms} integrals, with a saturation that sets the 1050 kHz limit of Fig. 3(b) of [1]. The oscillator follows $f = f_0\, e^{kv}$ with the measured small-signal slope; the exponential law is taken from the SKY130 rebuild, and it is the only law under which the measured 694 kHz swing at 2 mV_{pp} fits around a 245 kHz carrier. The body channel is a flat loss with 20 $nV/\sqrt{Hz}$ of receiver input noise, and spikes are detected after a 300 Hz to 6 kHz band-pass at 4.5 σ (median absolute deviation) and scored against the ground truth (F1).

Prior to any modification, the model reproduces the carrier for a 50 μV_{pp} input (237.0 to 254.3 kHz against 237 to 254 kHz), the spike-band noise (5.51 against 5.55 μV_{rms}) and the dynamic range (42.16 against 42.1 dB), and follows the published swing against amplitude and frequency (Fig. 2). Two SKY130 rebuilds of the ring of Fig. 2(c) of [1] supply the sensitivities. The first keeps the Table 1 sizes and ±0.6 V; as SKY130 thresholds are higher than those of the 180 nm process, it runs at 7.14 kHz instead of 245 kHz, and it is the baseline for **P10**. The second uses ±0.9 V and shorter inverters to sit near 240 kHz, with per-device Pelgrom mismatch over 24 Monte Carlo chips, and is the baseline for **P2** to **P7**.

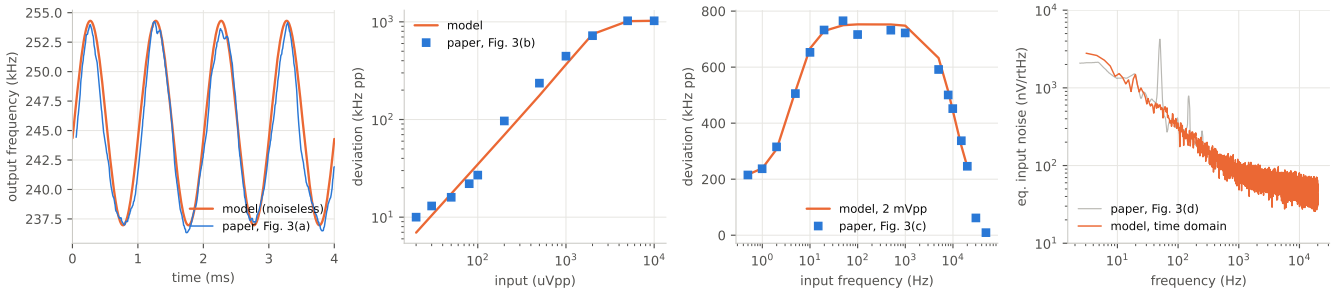


Figure 2: Validation against Fig. 3 of [1]: output frequency for a 50 μV_{pp} input, frequency deviation against input amplitude and against input frequency, and input-referred noise. Lines: model; markers and thin line: published data.

3 Limitations of the Published Design

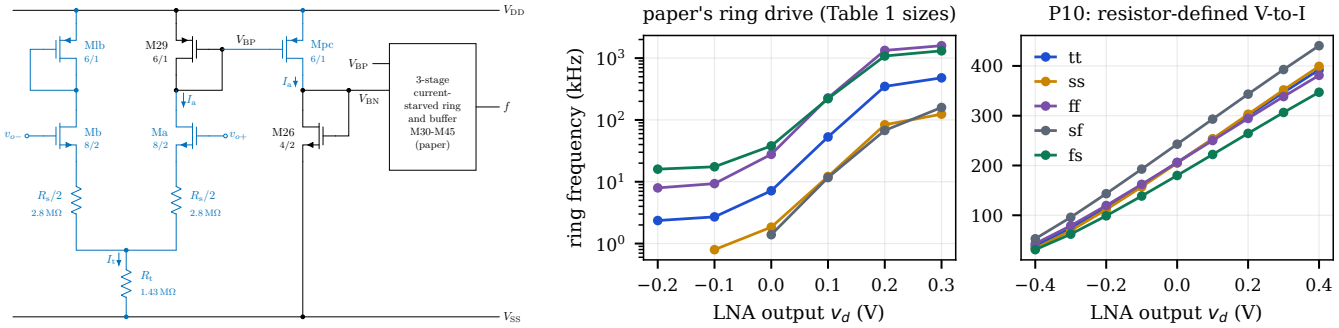
The published read-out assumes $f = f_0 + K_{vf} v$. In the SKY130 rebuild the ring itself is nearly linear in its current (3.09 to 3.41 kHz/nA from 10 to 320 nA); the error arises in the step that turns the LNA voltage into that current. The control transistors M27 and M28 operate in weak inversion, so the ring current, and with it both f_0 and K_{vf}, is exponential in the threshold voltage. At the Table 1 sizes the centre frequency spreads by a factor of 27.3 across the five SKY130 corners and moves by 7.05 %/°C (Fig. 3(b), left). With

the published linear read-out, the gain seen by the receiver changes by 4.0 %/°C (Fig. 4(a)), so a warming of the vessel by 2 °C changes the recorded spike amplitudes by 7.2 %; the size of a spike also depends on the slow wave under it (Fig. 4(b)). A 1 % change of the supply appears as 42 µV at the input, and 1 mV of 50 Hz ripple on the rails as 6.9 μV_{pk}. At the receiver, zero-crossing counting fails once the carrier-to-noise ratio approaches the FM threshold, which in the model limits spike detection with F1 $\geq$ 0.9 to 75 dB of channel loss.

4 Proposed Techniques

4.1 Resistor-defined voltage-to-current drive (P10)

A source-degenerated NMOS pair with a resistor tail and a diode load replaces the load-balancing amplifier and the control transistors (Fig. 3(a)). The ring current then follows $I_a = I_t/2 + v_d/(R_s + 2/g_m)$, which is set by a resistor instead of the threshold voltage; I_a sets V_{BP} through M29 and, through a copy transistor Mpc, V_{BN} through M26, so the ring M30 to M45 is unchanged. On the faithful ±0.6 V port, the centre frequency spreads by 1.35× instead of 27.3× over the five corners, the gain by 1.20× instead of 19.1×, and the tuning curve becomes linear to 1.18 % of the span (Fig. 3(b)). The resistors ($R_s/2$ = 2.8 MΩ, R_t = 1.43 MΩ, high-resistance poly) take about 430 µm², a sixth of the published core, and the supply current falls from 1.73 to 1.42 µA.



(a) P10 in blue (W/L in µm). **(b)** Ring frequency against the LNA output, five corners.

Figure 3: P10 at transistor level, SKY130, ±0.6 V, 27 °C: (a) the drive, with the published ring as a block; (b) the published drive (left, log scale) and P10 (right, linear scale).

4.2 Logarithmic read-out (P2) and two rings (P4)

Because the ring is exponential, $\ln f = \ln f_0 + kv$ is linear in the input with a slope k that does not contain f_0. Reading $\ln f$ in the receiver, with no change to the implant, reduces the gain drift from 4.0 to 0.31 %/°C over the physiological range (Fig. 4(a)), makes the size of a spike nearly independent of the slow wave under it (spread 33 against 3.9 % on a 400 µV wave, Fig. 4(b)), and reduces the nonlinearity of the SKY130 tuning curve from 3.8 to 0.24 % of the span (Fig. 4(c)).

P4 adds a second ring driven by the other LNA output, which is the published bias stack and ring with V_{c+} and V_{c-} swapped. Then $\ln(f_A/f_B) = 2kv$: the signal adds and whatever moves both rings together, such as temperature, supply and the process corner, cancels. Over 24 Monte Carlo chips the gain spread falls from 5.6 % to 0.41 % without per-device calibration, a 1 % supply change appears as 0.26 instead of 42 µV (44 dB), and 1 mV of 50 Hz ripple as 0.04 instead of 6.9 μV_{pk} (Fig. 5(a)). The two carriers share the output stage and the electrode. The ratio of the two carriers at rest is set by mismatch and does not move with temperature, so it identifies the implant (P7): after enrolment at 37 °C, 88 % of 24 chips are identified at 41 °C, against 4 % with the centre frequency of a single ring (Fig. 5(b)).

4.3 A phase-locked loop per carrier (P5)

A zero-crossing counter takes in the full noise bandwidth of its band-pass filter, so its output degrades abruptly at the FM threshold. A second-order digital PLL after a complex down-mix (40 kHz loop) only admits noise near the instantaneous frequency, which moves the threshold to a higher loss. With one ring,

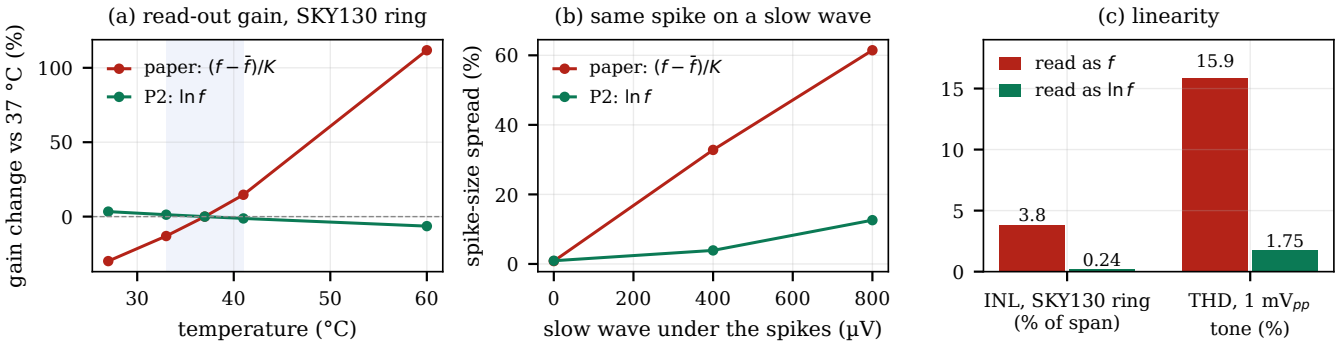


Figure 4: P2, behavioural model with the SKY130 ring (±0.9 V): (a) read-out gain against temperature relative to 37 °C (shaded: 33 to 41 °C); (b) spread of the recovered spike amplitude against the amplitude of the slow wave under the spikes; (c) nonlinearity of the SKY130 tuning curve and distortion of a 1 mV$_{pp}$ tone, read as f and as ln f.

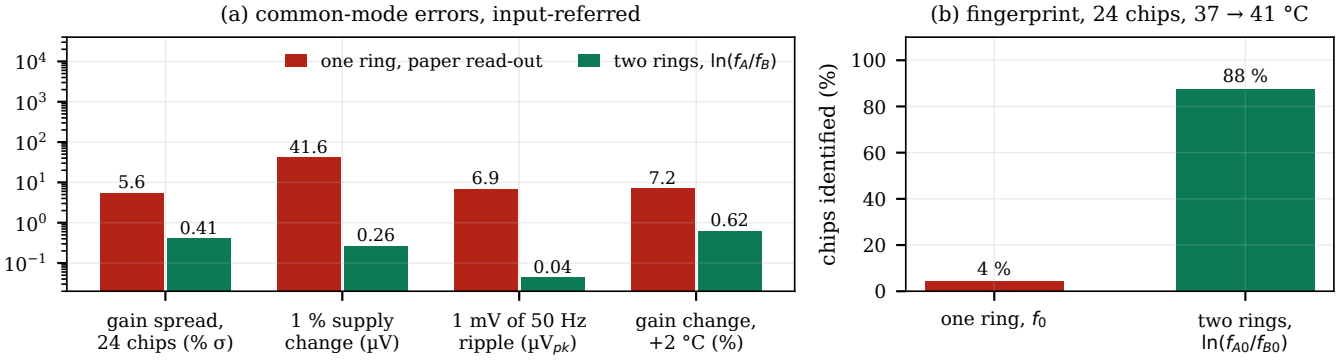


Figure 5: P4 and P7, behavioural model with 24 SKY130 Monte Carlo chips: (a) gain spread, supply pick-up, rail ripple and gain change for a 2 °C rise, input-referred, one ring with the published read-out against two rings read as $\ln(f_A/f_B)$ (log scale); (b) chips identified after a 4 °C change, from the centre frequency of one ring and from the ratio of the two carriers at rest.

the highest channel loss at which spikes are still detected with F1 ≥ 0.9 rises from 75 to 80 dB (Fig. 6(a), (b)). With P2, P4 and P5 together, a 2 °C temperature rise and 1 mV of rail ripple, the F1 score at 80 dB is 0.99 instead of 0.82 (Fig. 6(c)). Past the threshold, at 85 dB, both links fail and the proposed one more so (F1 0.29 against 0.45), because its two carriers share the output drive.

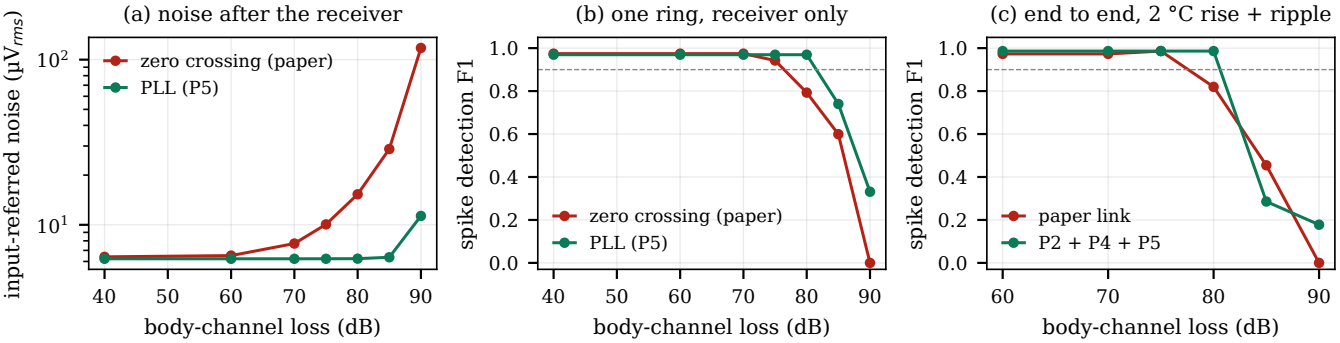


Figure 6: P5, behavioural model: (a) input-referred noise after the receiver and (b) spike-detection F1 against body-channel loss, one ring, zero-crossing counter against PLL; (c) end to end with a 2 °C rise and 1 mV of 50 Hz rail ripple, published link against P2, P4 and P5 together. Dashed: F1 = 0.9.

4.4 Further techniques (P11, P6)

A test tone of ±25 µV at the carrier frequency divided by 256 (959 Hz), injected at the LNA input, lets the receiver re-measure K_{vf} during recording: after a −20 % step in gain the estimate is within 1.19 % after 1 s and 0.24 % after 3 s, and the same tone measures the electrode impedance to within 0.72 % (Fig. 7(a)). Removed in the cycle domain, the tone leaves spike detection unchanged (F1 0.989 against 0.985 without

the tone). Lowering the gain of the diode stage by 8 (P6) reduces the Carson bandwidth of a 500 µV spike from 518 to 59 kHz, so that 15 implants fit into 100 kHz to 1 MHz instead of 1; with four implants on one channel, the worst F1 rises from 0.81 to 0.96 (Fig. 7(b)). The cost is an 8 times larger contribution of the oscillator noise referred to the input. A reciprocal counter (P1) further reduces the counting noise of a fixed 50 µs gate from 23.1 to 0.17 μV_{rms}.

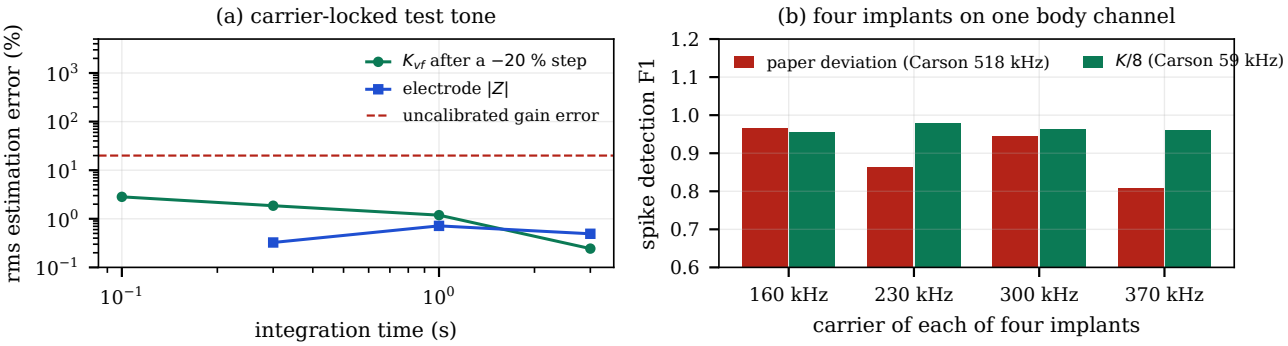


Figure 7: Further techniques: (a) P11, rms error of the K_{vf} and electrode-impedance estimates against integration time (dashed: gain error without calibration), implant-side model; (b) P6, spike-detection F1 of four implants sharing one body channel at the published deviation and at $K/8$, behavioural model.

5 Limits of This Study and Next Steps

SKY130 is not the 180 nm process of [1], so the absolute numbers will differ on the real chip, and the exponential law of the published ring is an inference from the measured 694 kHz swing around a 245 kHz carrier. The resistor mismatch and noise of P10 are not yet simulated, the body channel is a flat loss with white receiver noise, and the phase noise of the oscillator (−75 dBc/Hz at 10 kHz) is assumed. The first experimental check would be to measure $f(v)$ of the existing chip at 33 to 41 °C, and to apply the $\ln f$ read-out of P2 to existing recordings, which requires no new silicon.

References

[1] A. Meimandi, P. S. Crovetti, E. Citraro, F. P. Andriulli and S. Carrara, "A 0.0025 mm^2 CMOS neural front-end with VCO-based frequency encoding for body-coupled communication," *IEEE Sensors Lett.*, vol. 10, no. 9, 6008404, 2026, doi:10.1109/LSENS.2026.3716537.